International Journal of Research and Technology in Electrical Industry

journal homepage: ijrtei.sbu.ac.ir

Shahid Beheshti University

# Robust Vehicle Stability Control Using Smooth Sliding Mode and Tire Slip-Based Dynamic Control Allocation in ESC Systems

Mohammad Mirzaei[1], Ahmadreza Vali[1], Firouz Alahvirdizadeh[1], Vahid Behnamgol[2] *

[1] *Department of Electrical and Computer Engineering, Malek Ashter University of Technology, Tehran, Iran*
[2] *Energy Research Centre, Damavand Brach, Islamic Azad University, Damavand, Iran*

ARTICLE INFO

**Article history:**
Received: 07 September 2024
Revised: 20 November 2024
Accepted: 21 November 2024

**Keywords:**
Sliding Mode Control
Vehicle stability Control
Control Allocation
Chattering
Tire Slip Control



ABSTRACT

This paper presents a comprehensive study on a chattering-free sliding mode control designed to enhance vehicle lateral stability. The proposed control architecture is composed of three main components: an upper controller, a control allocation layer, and a lower controller. In the upper controller, using a smooth integral sliding mode controller, the desired yaw moment is designed for vehicle lateral stability and to guarantee the robust performance of the vehicle in the presence of uncertainties. In the middle layer, a dynamic control allocation with an analytical solution and based on the Lyapunov function is proposed for the distribution of desired longitudinal tire slip, which guarantees the optimality and convergence of them to the optimal set and also the asymptotic stability of the dynamics control allocation layer. And finally, in the lower layer, using the sliding mode controller, the brake torque is designed to track the longitudinal slip obtained from the dynamics control allocation layer. The main feature of the proposed control structure is considering practical considerations in terms of computational load in the control allocation layer, unlike numerical optimization methods, and also the compatibility of the designed ESC control with production vehicles due to the design of control allocation based on longitudinal slip and the use of ABS system based on longitudinal tire slip control. The 10-degree-of-freedom vehicle dynamics model is validated with CarSim and the simulation results of the proposed control for the DLC steering scenario show its effectiveness in terms of eliminating chattering, tracking accuracy compared to the conventional sliding mode control.

## 1. Introduction

To ensure stability and maneuverability during dynamic driving, vehicles use lateral stability control systems like Active Steering Control (ASC), Torque Vectoring Differential (TVD), and Electronic Stability Control (ESC). ASC is limited under extreme steering due to tire force constraints. TVD and ESC enhance control by distributing tire forces to regulate yaw moment. TVD improves handling in normal driving, while ESC, using brakes, prevents understeer and oversteer. ESC,

* Corresponding author
*E-mail address:* vahid_behnamgol@damavandiau.ac.ir
https://orcid.org/0000-0003-3555-8453
http://dx.doi.org/10.48308/ijrtei.2024.236831.1058

mandated since the early 2010s, is crucial for vehicle safety [1, 2].

vehicles often need an additional layer to interface with the ABS module within the ESC system, using longitudinal slip control for each wheel to design braking torques [6, 7]. Alternatively, braking pressure can be applied proportional to the CA output, ignoring wheel dynamics [8, 9].

The CA problem in related research can be categorized into three methods: optimization-based, experience-based, and Lyapunov-based. In optimization-based methods, the CA problem is formulated as a static optimization problem such as unconstrained linear or quadratic programming. In [10], a closed-form solution is presented for distributing forces and torques in vehicle dynamic control using unconstrained linear optimization. The main advantage of this method is its simplicity, but it is only applicable to linear problems and due to the lack of considering constraints, actuator saturation may occur. Numerical optimization methods with different solution methods have also been frequently used in research related to the distribution of vehicle forces and torques, with the WLS method [11, 12] being the most popular. Although these methods calculate the optimal solution accurately, achieving it requires solving the problem iteratively at each time step, which leads to computational complexity and implementation difficulties. Moreover, since most optimization-related research, due to not considering dynamics and changes related to actuators, is referred to as static methods, MPC is proposed to solve this problem [13], which has a high computational load. In experience-based methods such as fuzzy [14], the solution is based on expertise, which, despite its simplicity, does not guarantee optimality. In addition to the mentioned disadvantages of the two optimization-based and experience-based CA solution methods, due to the use of a multilayer structure in control loops along with CA, the inability to analyze stability despite the provided solution with these methods is another challenge. To address the mentioned challenges, the Lyapunov-based CA method is proposed, which guarantees optimality and convergence of the control signal to the optimal value by using the Lyapunov function and providing an analytical solution [15]. In fact, in this method, the layer related to the CA problem is considered similar to a subsystem. This method has been used in [16] to propose a near-optimal and dynamically distributed force distribution for electric vehicles, and in [17] to increase the convergence rate of brake force distribution among tires. The aforementioned method has also been used in aircraft applications [18] and fault tolerance [19].

Various control techniques, including MPC [20], fuzzy logic [21], and PI control [6], fixed-time nonlinear control [17], have been employed in the upper control layer for vehicle stability. However, fuzzy control lacks formal stability and convergence time proofs, PI control is susceptible to nonlinearities, and MPC exhibits limited robustness to uncertainties. sliding mode control (SMC) has become the predominant approach due to its effectiveness in handling nonlinear dynamics and uncertainties, such as terminal [22] and integral [23] sliding mode controllers. The presence of a signum function in the control input derived from first-order sliding mode control results in chattering. This phenomenon, caused by the inability of real-world actuators to switch instantaneously, leads to high-frequency oscillations in the control signal and is a primary challenge in SMC design [24]. To address this, researchers have explored continuous approximation [7] that replaces sign function with tanh(.), super-twisting algorithm [25] that uses second derivative of sliding variable and adaptive sliding mode method that reduces chattering by estimating uncertainties and avoiding high-gain terms [26].

This paper proposes a novel three-layer control structure for ESC systems, specifically designed to address practical constraints in production vehicles under critical road conditions. The upper layer employs a Smooth-Integral Sliding Mode Control (smooth-ISMC) to generate the desired vehicle yaw moment, robustly handling uncertainties. Key advantages of this approach include reduced chattering and improved steady-state tracking of the desired yaw rate. In the middle layer, a Dynamic Control Allocation (DCA) strategy is devised to distribute the desired torque among individual wheels based on their longitudinal slip. Leveraging Lyapunov stability theory, the proposed DCA offers a computationally efficient solution with guaranteed convergence to the optimal allocation, while considering practical constraints. The lower layer, responsible for brake actuation, utilizes a SMC to track the desired longitudinal slip dictated by the DCA. A detailed 10-DOF vehicle model is employed for simulations, validated against the comprehensive CarSim software. Simulation results for the Double Lane Change (DLC) maneuver demonstrate the superior performance of the proposed structure compared to a conventional approach employing SMC in both upper and lower layers, along with a weighted Pseudoinverse CA.

## 2. Vehicle Dynamic model

This research introduces a comprehensive 10-DOF vehicle model, including 6-DOF associated with in-plane motion and 4-DOF related to wheel spin. Steering constraints are considered, limited to the front axle. Vehicle chassis coordinate system $(x_b, y_b, z_b)$ adheres to the SAE convention. The inertia system, which remains fixed, aligns with the vehicle's initial direction $(X, Y, Z)$. Additionally, the undercarriage coordinate system $(x_{Un}, y_{Un}, z_{Un})$, representing the vehicle's center of mass projected onto the road surface, tracks translational motion and the vehicle's yaw angle. Fig. 1 illustrates the directions of the forces in both the vehicle chassis coordinate system and the wheels [17].

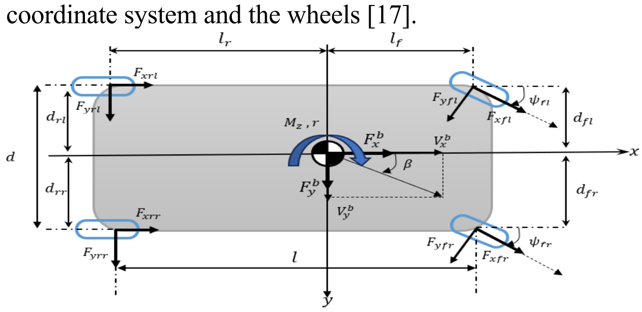

**Fig. 1.** Coordinates of the chassis and wheels on the plane [17].

### 2.1. Model Equations

The translational motion of the vehicle's center of mass (CoM) can be divided into translational and oscillatory components. The oscillatory component is due to the vehicle's suspension system. The translational motion equations are typically formulated as follows:

$$\boldsymbol{F^I} = \dot{\boldsymbol{P}} = \boldsymbol{M}\frac{\partial \boldsymbol{\mathcal{V}}}{\partial \boldsymbol{t}}, \boldsymbol{F^I} = \boldsymbol{T^I_{\mathcal{U}n}}(-\boldsymbol{\psi})\begin{pmatrix} F_x^{\mathcal{U}n} \\ F_y^{\mathcal{U}n} \\ F_z^{\mathcal{U}n} \end{pmatrix}$$

$$\boldsymbol{M} = \begin{pmatrix} m & 0 & 0 \\ 0 & m & 0 \\ 0 & 0 & m_s \end{pmatrix}$$

$$F_x^{\mathcal{U}n} = f^w_{x,fr}\, c_{\psi_{fr}} + f^w_{y,fr}\, s_{\psi_{fr}} + f^w_{x,fl}\, c_{\psi_{fl}} + f^w_{y,fl}\, s_{\psi_{fl}} + f^w_{x,rr} + f^w_{x,rl}$$

$$F_y^{\mathcal{U}n} = -f^w_{x,fr}\, s_{\psi_{fr}} + f^w_{y,fr}\, c_{\psi_{fr}} - f^w_{x,fl}\, s_{\psi_{fl}} + f^w_{y,fl}\, c_{\psi_{fl}} + f^w_{y,rr} + f^w_{y,rl} \quad (1)$$

The vertical component $F_z^{\mathcal{U}n}$ is expressed as follows:

$$\boldsymbol{F_z^{\mathcal{U}n}} = \boldsymbol{W_w} + \boldsymbol{fs}_{\boldsymbol{z}}^{\boldsymbol{\mathcal{U}n}},$$
$$\boldsymbol{fs^{\mathcal{U}n}} = \boldsymbol{S} + \boldsymbol{D} = [\boldsymbol{fs}_{\boldsymbol{fr}} \quad \boldsymbol{fs}_{\boldsymbol{fl}} \quad \boldsymbol{fs}_{\boldsymbol{rr}} \quad \boldsymbol{fs}_{\boldsymbol{rl}}] \quad (2)$$

$F_z^{\mathcal{U}n}$ describes the vertical suspension force which consists of two components: a static component, $W_w$, and a dynamic component resulting from the suspension system's response to road conditions. This paper primarily focuses on the vertical component of the suspension force vector, neglecting the relatively small horizontal component. The vertical component of the suspension force vector, denoted as $fs^{\mathcal{U}n}$. In (1), S, representing the spring force, and D, which is a matrix representing the damper force vectors. In the case of a suspension system with linear springs, the spring force is initially calculated in the body coordinate system and then transformed into the undercarriage coordinate system.

$$\boldsymbol{S} = \boldsymbol{T_b^{\mathcal{U}n}} \begin{bmatrix} k_{fr} & k_{fl} & k_{rr} & k_{rl} \\ k_{fr} & k_{fl} & k_{rr} & k_{rl} \\ k_{fr} & k_{fl} & k_{rr} & k_{rl} \end{bmatrix} \boldsymbol{\Delta},$$

$$\boldsymbol{D} = \boldsymbol{T_b^{\mathcal{U}n}} \begin{bmatrix} c_{fr} & c_{fl} & c_{rr} & c_{rl} \\ c_{fr} & c_{fl} & c_{rr} & c_{rl} \\ c_{fr} & c_{fl} & c_{rr} & c_{rl} \end{bmatrix} \odot \dot{\boldsymbol{\Delta}}_c$$

$$\boldsymbol{T_b^{\mathcal{U}n}}(-\square, -\theta) = \begin{bmatrix} C_\theta & 0 & S_\theta \\ 0 & 1 & 0 \\ -S_\theta & 0 & C_\theta \end{bmatrix} \begin{bmatrix} 1 & 0 & 0 \\ 0 & C_\varphi & -S_\varphi \\ 0 & S_\varphi & C_\varphi \end{bmatrix}$$

$$\boldsymbol{\Delta} = \boldsymbol{R_w^b} - \boldsymbol{R_{0w}^b} = \boldsymbol{T^b_{\mathcal{U}n}}(\boldsymbol{R^b_{0w}} - \boldsymbol{\mathcal{R}}) - \boldsymbol{R^b_{0w}}$$

$$\boldsymbol{R^b_{0w}} = \begin{bmatrix} l_f & l_f & -l_r & -l_r \\ d_{fr} & -d_{fl} & d_{rr} & -d_{rl} \\ h - r_w & h - r_w & h - r_w & h - r_w \end{bmatrix}$$

$$\boldsymbol{\mathcal{R}} = \begin{bmatrix} 0 & 0 & 0 & 0 \\ 0 & 0 & 0 & 0 \\ z^I - h & z^I - h & z^I - h & z^I - h \end{bmatrix} \quad (3)$$

$\dot{\boldsymbol{\Delta}}_c$, containing the velocities of suspension displacement within the chassis system [17]. The longitudinal and lateral friction forces acting on each wheel, $f^w_{x,y,ij}$, are determined relative to the wheel velocity coordinate using the Burckhardt model [27].

Using the magnitude of angular momentum, we derive the equations for rotational motion from the subsequent relationship:

$$\boldsymbol{M} = (\boldsymbol{M_f^b} + \boldsymbol{M_{y_w}^b} + \boldsymbol{M_s^b}) = \boldsymbol{I}\frac{\partial \boldsymbol{\omega}}{\partial \boldsymbol{t}} + \boldsymbol{\omega} \times \boldsymbol{I\omega},$$

$$\boldsymbol{I} = \begin{bmatrix} I_x & 0 & 0 \\ 0 & I_y & 0 \\ 0 & 0 & I_z \end{bmatrix} \quad (4)$$

$M_f^b$, $M_{y_w}^b$, and $M_s^b$ represent the tire-ground friction on the wheel plane, perpendicular tire-ground friction, and dynamic vertical forces, respectively and are calculated as follows:

$$\boldsymbol{M_f^b} = \sum_{ij} \boldsymbol{R_w^b} \otimes \boldsymbol{F^b_{x_w}}, \boldsymbol{F^b_{x_w}} = [\boldsymbol{f^b_{fr}} \quad \boldsymbol{f^b_{fl}} \quad \boldsymbol{f^b_{rr}} \quad \boldsymbol{f^b_{rl}}]$$

$$\boldsymbol{M^b_{y_w}} = \sum_{ij} \boldsymbol{R_c^b} \otimes \boldsymbol{F^b_{y_w}}, \boldsymbol{F^b_{y_w}} = [\boldsymbol{f^b_{y_{fr}}} \quad \boldsymbol{f^b_{y_{fl}}} \quad \boldsymbol{f^b_{y_{rr}}} \quad \boldsymbol{f^b_{y_{rl}}}]$$

$$\boldsymbol{f^b_{y_w}} = \boldsymbol{T}(\varphi)\boldsymbol{T}(\theta)\boldsymbol{T}(-\psi_w)\begin{pmatrix} 0 \\ f_y{}^w \\ 0 \end{pmatrix}$$

$$\boldsymbol{R_c^b} = \boldsymbol{T^b_{\mathcal{U}n}}(\boldsymbol{R^b_{0c}} - \boldsymbol{\mathcal{R}})$$

$$\boldsymbol{T^b_{\mathcal{U}n}} = \boldsymbol{T}(\varphi)\boldsymbol{T}(\theta), \boldsymbol{R^b_{0c}} = \begin{bmatrix} l_f & l_f & -l_r & -l_r \\ d_{fr} & -d_{fl} & d_{rr} & -d_{rl} \\ h & h & h & h \end{bmatrix}$$

$$\boldsymbol{M_s^b} = \sum \boldsymbol{R_w^b} \otimes \boldsymbol{fs^b}, \boldsymbol{fs^b} = \boldsymbol{T^b_{\mathcal{U}n}}\ \boldsymbol{fs^{\mathcal{U}n}} \quad (5)$$

The dynamic equation for each wheel rotation can be obtained as follows:

$$J_w \dot{\omega}^w_{ij} = Tb_{ij} - r_{w_{ij}} f x^w_{ij},\ ij = fr, fl, rr, rl \quad (6)$$

where $\omega^w_{ij}$ represents the angular velocity of each wheel in the wheel frame, and $Tb_{ij}$ denotes the braking torque.

### 2.2. Reference Model

The design of the upper layer controller within an ESC system is contingent upon the key target yaw rate variable [9]:

$$r_{ref} = \frac{V_x}{l + K_{us}{V_x}^2}\delta, \quad K_{us} = \frac{m}{2l}\left(\frac{l_r}{C_{\alpha f}} - \frac{l_f}{C_{\alpha r}}\right) \quad (7)$$

The parameter $K_{us}$ represents the vehicle's understeer gradient, a critical factor affecting its steering behavior. Moreover, the desired yaw rate is constrained by the vehicle's maximum lateral acceleration, which relies on the road friction coefficient. Reference [9] establishes an upper bound, $r_{upper_{bound}} = 0.85\frac{\mu g}{V_x}$. Consequently, the final desired yaw rate is determined using the following relation:

$$r_d = \begin{cases} r_{ref} & , |r_{ref}| \leq r_{upper_{bound}} \\ r_{upper_{bound}} & sgn(r_{ref}), |\dot{r}_{ref}| > r_{upper_{bound}} \end{cases} \quad (8)$$

Additionally, the actual vehicle sideslip angle, β, is constrained to be less than or equal to $\beta_{upper\_bound}$, which is calculated as:

$$\beta_{upper\_bound} = tan^{-1}(0.02\mu g) \quad (9)$$

This limits the maximum permissible vehicle side slip angle to approximately 12 degrees on dry asphalt roads.

### *2.3. Validation of the 10-Degree-of-Freedom Dynamic Model of the Car with CarSim Software*

The accuracy of the proposed dynamic vehicle model, developed in MATLAB/ Simulink, is assessed by comparing its simulation results with those obtained from the industry-standard CarSim software. Both models are subjected to an identical steering maneuver and braking scenario: a left turn initiated with a 15-degree steering angle, peaking at 30 degrees, while applying 20 bar and 40 bar brake pressure to the front and rear wheels, respectively. The simulation is conducted at a speed of 100 km/h on a dry road. The vehicle's dynamics parameters are presented in Table I.

**Table I.** vehicle parameters.

| Parameters | Value | Parameters | Value |
|---|---|---|---|
| $m$ | $1791\ kg$ | $l$ | $2720\ mm$ |
| $m_w$ | $25\ kg$ | $d_f$ | $1552\ mm$ |
| $g$ | $9.81\ ^{m}/_{s^2}$ | $d_r$ | $1560\ mm$ |
| $I_x$ | $1030\ kg.m^2$ | $k_{ij}$ | $50\ ^{N}/_{mm}$ |
| $I_y$ | $1200\ kg.m^2$ | $c_{ij}$ | $2\ ^{N.s}/_{mm}$ |
| $I_z$ | $1230\ kg.m^2$ | $r_{w_{fr}} = r_{w_{fl}}$ | $0.292\ m$ |
| $w_{fr}$ | $5165.6\ N$ | $r_{w_{rr}} = r_{w_{rl}}$ | $0.296\ m$ |
| $w_{fl}$ | $5023.6\ N$ | $r_{p_{fr}} = r_{p_{fl}}$ | $0.145\ m$ |
| $w_{rr}$ | $3720\ N$ | $r_{p_{rr}} = r_{p_{rl}}$ | $0.130\ m$ |
| $w_{rl}$ | $3706\ N$ | $\mu_{p_{ij}}$ | $0.4$ |
| $C_{\alpha f}$ | $1800\ ^{N}/_{deg}$ | h | *754 mm* |
| $C_{\alpha r}$ | $1900\ ^{N}/_{deg}$ | | |

Fig. 2 illustrates the linear displacement and velocity at the vehicle's center of mass. Both the Simulink and CarSim models demonstrate comparable behavior and movement patterns in the horizontal plane. However, a minor discrepancy of approximately 5 cm is observed in the vertical axis displacement at the onset of the scenario, likely due to variations in the suspension system modeling between the two models.

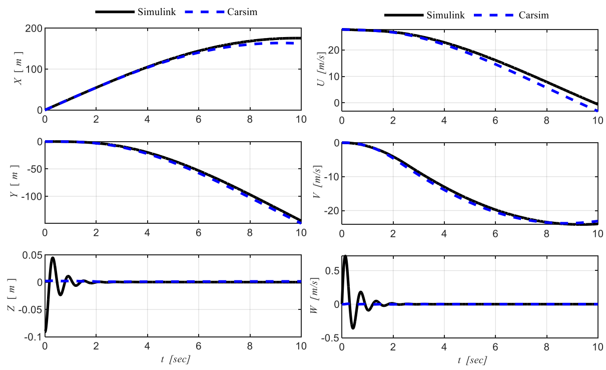


Fig. 2. Position (left) and vehicle velocity (right) vector components of the center of mass of the vehicle in the inertial frame.

The angular velocity components in the chassis frame are depicted on the right side of Fig. 2. A strong correlation is evident among all three components, particularly between the p and r components. These values exhibit a high degree of similarity. The disparity in vertical load distribution between the front and rear axles in the two models, coupled with the displacement of the center of mass, has led to variations in the twist angle rate. The suspension mechanism's structural differences between the front and rear axles can contribute to distinct behaviors, especially in the steering axle.

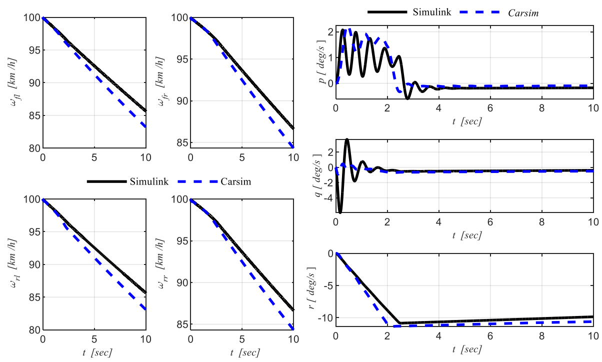


**Fig. 3.** Linear velocity of the wheels (left) and angular velocity of the vehicle chassis (right).

The left side of Fig. 3 illustrates the linear velocity of the wheel circumference, which follows consistent trends across all wheels. The minor discrepancies observed between the two models can be attributed to the Simulink model's assumption of rigid wheels and the CarSim model's consideration of malleability and dynamic changes in the effective wheel radius. As a result, the speed variations are slightly more pronounced in the CarSim model.

## 3. Proposed control structure

The proposed control architecture, illustrated in Fig. 4, is a three-layer hierarchical structure. An upper controller calculates the desired yaw moment based on the reference yaw rate, which is then distributed among the tires using optimal control allocation. The lower controller tracks the desired slip using brake torque.

Assuming available sensor data, a state estimator provides necessary vehicle information. The control design prioritizes vehicle stability in the presence of model uncertainties.
The hierarchical control structure, consisting of a upper controller, a control allocation layer, and a lower controller, is formulated and designed in the following sections.

### 3.1. Problem Formulation

The over-actuated nonlinear system can be represented in the following affine form:

$$\dot{r} = \frac{Mz^y}{I_z} + \frac{1}{I_z} M_z{}^x \tag{10}$$

$$M_z{}^x = [l_f S_\delta - d_{fr} C_\delta \quad l_f S_\delta + d_{fl} C_\delta \quad -d_{rr} \quad d_{rl}] \begin{bmatrix} f_{x,fr}^w \\ f_{x,fl}^w \\ f_{x,rr}^w \\ f_{x,rl}^w \end{bmatrix},$$

$$f_{x_{ij}}^w = C_{x,ij}\, \lambda_{x_{ij}}, ij = fr, fl, rr, rl \tag{11}$$

$$\min J(u) = \frac{1}{2} u^T W_u u \qquad s.t: \underline{u}_{ij} \le u \le \overline{u}_{ij},$$
$$u = \begin{pmatrix} \lambda_{x_{fr}} & \lambda_{x_{fl}} & \lambda_{x_{rr}} & \lambda_{x_{rl}} \end{pmatrix}^T \tag{12}$$

Equation (10) represents the upper control system, which generates a virtual control signal. Since this signal cannot be directly applied to the actuators, it is mapped to the desired actuator inputs and longitudinal slip through (11). $C_{x,ij}$ denotes to longitudinal stiffness in linear friction forces model [9]. Finally, (12) defines constraint bounds on the actuator-related variable (longitudinal slip) to ensure longitudinal friction force operation within the stable region and introduces the cost function $J_1$ for minimizing the actuator (braking) control effort. In this equation, the $W_{u_1}$weighting matrix is a diagonal matrix of dimension $R^{4\times4}$. Since the number of actuator inputs $(u)$ is greater than the virtual control signal, dynamic control allocation is employed to resolve the issue of actuator input non-uniqueness in the mapping of (11) with respect to the requested $M_z{}^x$. Consequently, the design of the virtual control $M_z{}^d$ is addressed, followed by the distribution of the desired actuator inputs, longitudinal slip, using the proposed control allocation method.

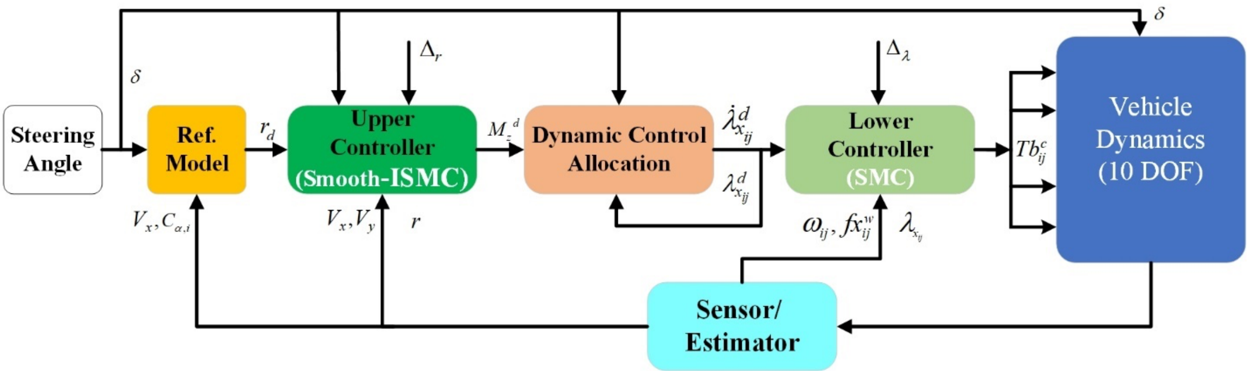


**Fig. 4.** Proposed Control Schematic for the ESC Vehicle System

### 3.2. Upper Controller

This section designs a controller for the virtual control input $M_z{}^x$ based on (10) dynamic system. The controller tracks the reference signal $(r_d)$. Equation (10) expresses the yaw moment $Mz^y$ obtained by approximating lateral forces using bicycle model relationships [9]:

$$\hat{f}_{y,fj}^w = C_{\alpha f}\beta_{fj} = C_{\alpha f}.\left(\delta - \frac{v_y + l_f r}{v_x}\right)$$
$$\hat{f}_{y,rj}^w = C_{\alpha r}\beta_{rj} = C_{\alpha r}.\left(-\frac{v_y + l_f r}{v_x}\right),$$
$$j = r, l \tag{13}$$

By defining the state error as $e_r = r - r_d$, the overall upper controller dynamics can be expressed as:

$$\dot{e}_r = \hat{f}_r(\beta, r) + \frac{1}{\hat{I}_z} M_z{}^x + \Delta_r, |\Delta_r| \le R \ge 0 \tag{14}$$

Where $\hat{f}_r = \frac{\hat{M}z^y}{\hat{I}_z} - \dot{r}_d$ and $\Delta_r$ is bounded by the approximation error in the lateral forces and the uncertainty in the $\hat{I}_z$ parameter.

**Theorem 1:** Consider the nonlinear system (14) with a sliding surface defined as $s_r = e_r + k_I \int e_r$ . The proposed ***smooth Integral Sliding Mode Controller*** (15) ensures finite-time convergence of the sliding surface $s_r$ with a reaching time of $t_r$.

$$M_z{}^d = -\hat{I}_z\big(\hat{f}_r(\beta, r) + \alpha\, sign(s_r) + \eta\, |s_r|^\gamma sign(s_r) + k_I\, e_r\big),$$
$$0 < \gamma < 1, \;\; \alpha, \eta, k_I > 0 \tag{15}$$

**Proof:** Considering the Lyapunov function $V_r = \frac{1}{2} s_r{}^2$, its time derivative is given by:

$$\dot{V}_r = s_r \dot{s}_r = s_r \left(\hat{f}_r(\beta, r) + \frac{1}{\hat{I}_z} M_z{}^x + \Delta_r + k_I\, e_r\right) \tag{16}$$

Substituting the control law from (15) into (16) yields:

$$\dot{V}_r = s_r\dot{s_r} = s_r(-\alpha\ sign(s_r) - \eta\ |s_r|^{\gamma} sign(s_r) + \Delta_r) \leq -\eta\ |s_r|^{\gamma+1} \quad (17)$$

In the preceding equation, $\alpha$ is selected as the maximum value of $\Delta_r$, equivalent to the upper bound of uncertainty, $R$. Hence, the sliding surface $s_r$ reaches to zero in finite time bounded by $t_r \leq \frac{|s_r(0)|^{1-\gamma}}{\eta(1-\gamma)}$ [28, 29]. Additionally, for $s_r = 0$, the yaw rate error $e_r$ converges asymptotically to zero, as $\dot{e}_r = -k_I\, e_r$.

**Remark:** To compare the performance of the proposed control method with the standard sliding mode control, we simultaneously examine the control inputs (u) designed by both methods as shown in Equation (18):

Conventional SMC:

$$u = u_{eq} - (\alpha + \eta)\, Sgn(S_r)$$

Proposed Smooth SMC:

$$u = u_{eq} - \alpha Sgn(S_r) - \eta S_r \left|S_r\right|^{\gamma-1} \quad (18)$$

In equation (18), $u_{eq}$ is equivalent control. As observed, the chattering amplitude in the proposed method is bounded by α and is significantly smaller than the chattering amplitude of the standard sliding mode control, which is bounded by α + η. Notably, the proposed method inherently produces smoother control signals for deterministic nonlinear systems. However, for uncertain nonlinear systems, additional techniques may be required to mitigate chattering. By employing continuous approximation and approximating the sign function with the Tanh(.) function, we obtain:

Approximated Conventional SMC:

$$u = u_{eq} - (\alpha + \eta)\, Tanh(S_r/\varepsilon)$$

Approximated Proposed Smooth SMC:

$$u = u_{eq} - \alpha Tanh(S_r/\varepsilon) - \eta S_r \left|S_r\right|^{\gamma-1} \quad (19)$$

Given the larger amplitude of the reaching phase in the standard sliding mode control approximation compared to the proposed method, a wider boundary layer near the sliding surface is necessary to ensure a smooth control signal and suppress chattering. Consequently, the proposed method allows for a narrower boundary layer, enabling more precise control. The standard sliding mode control, relying solely on a single term for both robustness and stability, often requires larger α values, leading to increased chattering. The proposed method addresses this limitation by incorporating the continuous reaching phase term, $\eta\ |s_r|^{\gamma}$, which provides a more flexible approach to tuning the control system's behavior. The parameter γ can be adjusted to fine-tune the reaching time and overall performance.

### 3.3. Proposed Dynamic Control Allocation

This paper presents a novel control allocation (CA) strategy for enhancing vehicle stability. To address the over-actuation problem arising from the distribution of a single desired yaw moment among four brake actuators, a Lyapunov-based dynamic control allocation (DCA) method is proposed. The primary objective of CA is to achieve the desired yaw moment, $M_z^{d}$, using brake actuators. To overcome the challenges associated with direct control of longitudinal tire forces, the proposed DCA method utilizes longitudinal slip information. A secondary objective is to minimize the control signal and ensure that the tire operates within its linear region. By imposing constraints on longitudinal slip, the DCA method can effectively distinguish between stable and unstable tire operating regions, as illustrated in Fig.5.

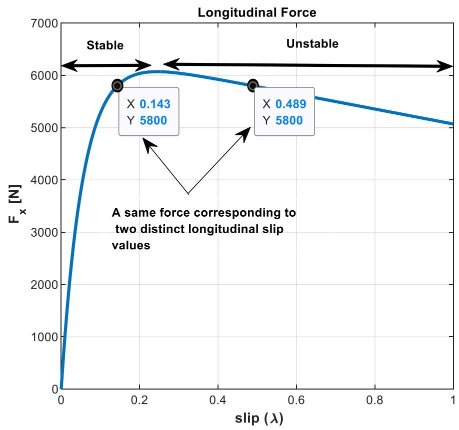


**Fig. 5.** Tire longitudinal force-slip characteristics

Based on primary objective of CA, the following constraint must be satisfied in the DCA problem considering the desired yaw moment $M_z^{\ d}$ as defined in Equation (15) and the relationship in Equation (11):

$$M_z^{\ d} - M_z^{\ x}(\delta, \boldsymbol{u_d}) = 0$$
$$\boldsymbol{u_d} = \left(\lambda_{x_{fr}}^{d} \quad \lambda_{x_{fl}}^{d} \quad \lambda_{x_{rr}}^{d} \quad \lambda_{x_{rl}}^{d}\right)^T \quad (20)$$

In the above equation, $u_d$ represents the desired longitudinal slip obtained from the control allocation. Based on (11), $M_z^{\ x}$ can be approximated as follows:

$$M_z^{\ x}(\delta, u_d) = \begin{bmatrix} l_f S_\delta - d_{fr} C_\delta & l_f S_\delta + d_{fl} C_\delta & -d_{rr} & d_{rl} \end{bmatrix} \begin{bmatrix} \lambda_{x_{fr}}^{d} \\ \lambda_{x_{fl}}^{d} \\ \lambda_{x_{rr}}^{d} \\ \lambda_{x_{rl}}^{d} \end{bmatrix} = B\, \boldsymbol{u_d} \quad (21)$$

In the aforementioned relationship, $\boldsymbol{u_d}$ represents the optimal longitudinal slip obtained from the DCA. Furthermore, as expressed in Equation (12), the constraint on tire longitudinal slip is incorporated as a penalty function in addition to minimizing the control effort ($J_1$). This constraint aims to ensure tire operation within the stable region of the tire-road longitudinal friction-slip curve. By minimizing this function, the desired longitudinal slip constraint is also satisfied. This function is then added to the cost function $J_1$:

$$min J(u_d) = J_1 + J_2$$
$$J_1(u_d) = \frac{1}{2} u_d{}^T W_{u_1} u_d \,,$$
$$J_2(u_d) = -W_{u_2} \sum_{k=1}^{2} \sum_{ij} P_{k,ij}(u_d) \tag{22}$$

where $P_{1,ij}(u_d) = \max\left(0, \left(\underline{u}_{ij} - u_{d_{ij}}\right)\right)^2$ and $P_{2,ij}(u_d) = \max\left(0, \left(u_{d_{ij}} - \overline{u}_{ij}\right)\right)^2$. In the aforementioned relationship, $W_{u_2}$ represents the weighting matrix. Consequently, the CA problem is formulated as follows:

$$\min J(u_d)$$
$$s.t \ : \ \ M_z{}^d - M_z{}^x(\delta, u_d) = 0 \tag{23}$$

By introducing the Lagrangian function as follows, we obtain:

$$\mathcal{L}(\boldsymbol{u_d}, \gamma, M_z{}^d) = J(\boldsymbol{u_d}) + \gamma\left(M_z{}^d - M_z{}^x(\delta, \boldsymbol{u_d})\right),\ \gamma \in R \tag{24}$$

Finding the solution to the CA optimization problem presented in (23) hinges on satisfying the first-order optimality conditions for the Lagrangian function defined in Equation (24) [30]. This ensures that we identify the optimal set, which can be expressed as follows:

$$\mathcal{S}_{CA}\,(\boldsymbol{u_d}, \gamma) = \left\{ (\boldsymbol{u_d}^T, \gamma) \middle| \frac{\partial \boldsymbol{\mathcal{L}}}{\partial \boldsymbol{u_d}} = 0 \,, \frac{\partial \mathcal{L}}{\partial \gamma} = 0 \right\} \tag{25}$$

Given the defined optimal set, $\mathcal{S}_{CA}$, this work aims to ensure that the proposed DCA algorithm achieves finite-time convergence to $\mathcal{S}_{CA}$. To this end, the Lyapunov function depicted below is employed for the DCA subsystem, as shown in [17].

$$V_{CA}(\boldsymbol{u_d}, \gamma, M_z{}^d) = \frac{1}{2} \begin{pmatrix} \frac{\partial \boldsymbol{\mathcal{L}}}{\partial \boldsymbol{u_d}}^T & \frac{\partial \mathcal{L}}{\partial \gamma} \end{pmatrix} \begin{pmatrix} \frac{\partial \boldsymbol{\mathcal{L}}}{\partial \boldsymbol{u_d}} \\ \frac{\partial \mathcal{L}}{\partial \gamma} \end{pmatrix} \tag{26}$$

To prove that a lemma is relevant to the DCA problem solution, we posit the following assumptions:

**Assumption 1:** $\mathcal{L}$ possesses a second derivative, $\frac{\partial^2 \boldsymbol{\mathcal{L}}}{\partial \boldsymbol{u_d}^2}$, and it satisfies the inequality $\kappa_1 \mathbb{I} \leq \frac{\partial^2 \boldsymbol{\mathcal{L}}}{\partial \boldsymbol{u_d}^2} \leq \kappa_2 \mathbb{I}$. Here, $\mathbb{I}$ denotes the identity matrix with the same dimension as the actuator's input, and $k_1$ and $k_2$ are positive constants.

**Assumption 2:** A positive constant $\varepsilon$ exists such that the matrix inequality $\frac{\partial (M_z{}^x)^T}{\partial u_d} \frac{\partial M_z{}^x}{\partial u_d} \geq \varepsilon I$ holds.

**Theorem 2:** Under the assumption of a $M_z{}^d$ controller designed following **Theorem 1**, Let us assume that the subsystem $\begin{pmatrix} \dot{u}_d \\ \dot{\gamma} \end{pmatrix}$ is proposed as follows:

$$\begin{pmatrix} \dot{u}_d \\ \dot{\gamma} \end{pmatrix} = -k_{CA} H^{-1} \begin{pmatrix} \frac{\partial \mathcal{L}}{\partial u_d} \\ \frac{\partial \mathcal{L}}{\partial \gamma} \end{pmatrix} + \begin{pmatrix} \varsigma \\ \chi \end{pmatrix} \tag{27}$$

Consequently, the optimal parameters $(\boldsymbol{u_d}, \gamma)$ converge to the optimal set $\mathcal{S}_{CA}$ asymptotically. For the relationship $\begin{pmatrix} \varsigma \\ \chi \end{pmatrix} \in R^5$ defined above, the auxiliary variables are uniquely achievable. Additionally, under Assumption 1 and **2**, matrix $\mathbf{H} = \begin{pmatrix} \frac{\partial^2 \mathcal{L}}{\partial u_d{}^2} & \frac{\partial^2 \mathcal{L}}{\partial \gamma \, \partial u_d} \\ \frac{\partial^2 \mathcal{L}}{\partial u_d \, \partial \gamma} & 0 \end{pmatrix}$ is invertible.

**Proof:**

Assuming an $M_z{}^d$ controller designed following Theorem 1 and convergence of $e_r \to 0$, the derivative of the Lyapunov function $V_{CA}(u_d, \gamma, M_z{}^d)$ can be expressed as:

$$\dot{V}_{CA}(\boldsymbol{u_d}, \gamma, M_z{}^d) = \begin{pmatrix} \frac{\partial \boldsymbol{\mathcal{L}}}{\partial \boldsymbol{u_d}}^T & \frac{\partial \mathcal{L}}{\partial \gamma}^T \end{pmatrix} \boldsymbol{H} \begin{pmatrix} \dot{\boldsymbol{u}}_{\boldsymbol{d}} \\ \dot{\gamma} \end{pmatrix} + \begin{pmatrix} \frac{\partial \boldsymbol{\mathcal{L}}}{\partial \boldsymbol{u_d}}^T & \frac{\partial \mathcal{L}}{\partial \gamma}^T \end{pmatrix} \begin{pmatrix} \frac{\partial^2 \boldsymbol{\mathcal{L}}}{\partial \boldsymbol{M_z{}^d} \ \partial \boldsymbol{u_d}} \\ \frac{\partial^2 \mathcal{L}}{\partial M_z{}^d \ \partial \gamma} \end{pmatrix} \dot{M}_z{}^d \tag{28}$$

In the above equation, $\frac{\partial^2 \mathcal{L}}{\partial M_z{}^d \ u_d} = 0^{4\times 1}$, and by selecting $\begin{pmatrix} \dot{u}_d \\ \dot{\gamma} \end{pmatrix}$ as per Eq. (27), we obtain:

$$\dot{V}_{CA}(u_d, \gamma, M_z{}^d) = -k_{CA} V_{CA} + \mathcal{F}(u_d, \gamma, M_z{}^d) + \begin{pmatrix} \frac{\partial \mathcal{L}}{\partial u}^T & \frac{\partial \mathcal{L}}{\partial \lambda}^T \end{pmatrix} H \begin{pmatrix} \varsigma \\ \chi \end{pmatrix} \tag{29}$$

Given that $\mathcal{F}(u_d, \gamma, M_z{}^d) = \begin{pmatrix} \frac{\partial \mathcal{L}}{\partial u_d}^T & \frac{\partial \mathcal{L}}{\partial \gamma}^T \end{pmatrix} \begin{pmatrix} \frac{\partial^2 \mathcal{L}}{\partial M_z{}^d \ \partial u_d} \\ \frac{\partial^2 \mathcal{L}}{\partial M_z{}^d \ \partial \gamma} \end{pmatrix} \dot{M}_z{}^d$. In following, is proofed that equation $\begin{pmatrix} \frac{\partial \mathcal{L}}{\partial u}^T & \frac{\partial \mathcal{L}}{\partial \lambda}^T \end{pmatrix} H \begin{pmatrix} \varsigma \\ \chi \end{pmatrix} + \mathcal{F}(u_d, \gamma, M_z{}^d) = 0$ always has a unique solution with respect to $\begin{pmatrix} \varsigma \\ \chi \end{pmatrix}$. We consider an auxiliary variable $\lambda_{\varsigma\chi}$ and define the Lagrangian function $\mathcal{L}_{\varsigma\chi}$ as:

$$\mathcal{L}_{\varsigma\chi} = \tfrac{1}{2}\varsigma^T \varsigma + \tfrac{1}{2}\chi^T \chi + \lambda_{\varsigma\chi}(\begin{pmatrix} \frac{\partial \mathcal{L}}{\partial u_d}^T & \frac{\partial \mathcal{L}}{\partial \gamma}^T \end{pmatrix} H \begin{pmatrix} \varsigma \\ \chi \end{pmatrix} + \mathcal{F}(u_d, \gamma, M_z{}^d) \tag{30}$$

To fulfill the first-order optimality conditions, $\mathcal{L}_{\varsigma\chi}$ must be stationary with respect to $(\varsigma, \chi, \lambda_{\varsigma\chi})$. This yields the system of equations:

$$\begin{pmatrix} I_{5\times5} & H^T\begin{pmatrix} \frac{\partial\mathcal{L}}{\partial u_d} \\ \frac{\partial\mathcal{L}}{\partial\gamma} \end{pmatrix} \\ \begin{pmatrix} \frac{\partial\mathcal{L}}{\partial u_d}^T & \frac{\partial\mathcal{L}}{\partial\gamma}^T \end{pmatrix} H & 0 \end{pmatrix}\begin{pmatrix} \varsigma \\ \chi \\ \lambda_{\varsigma\chi} \end{pmatrix} = \begin{pmatrix} 0_{5\times1} \\ -\mathcal{F}(u_d,\gamma,{M_z}^d) \end{pmatrix} \quad (31)$$

By Lemma 16.1 in [30], equation (31)'s left-hand side matrix is KKT and nonsingular, ensuring a unique solution for $\begin{pmatrix} \varsigma \\ \chi \\ \lambda_{\varsigma\chi} \end{pmatrix}$. Consequently, Eq. (28) is rewrited by following:

$$\dot{V}_{CA}(u_d,\gamma,{M_z}^d) \le -2k_{CA}V_{CA} \quad (32)$$

Consequently, according to (27) the optimal parameters $(u_d,\gamma)$ converge to the optimal set $\mathcal{S}_{CA}$ asymptotically.

### *3.4. Lower Controller*

The CA layer calculates the optimal longitudinal slip for each wheel. This desired slip is then achieved in the lower control layer by designing the control torque based on the optimal values. SMC is proposed for this task due to its robustness to model uncertainties and its ability to achieve finite-time tracking, enabling independent control of each wheel's slip. The governing equations for longitudinal slip ($\lambda_{x_{ij}} = \frac{V_x - r_{w_{ij}}.\omega_{ij}^w}{V_x}$) and its derivative for each wheel are presented as follows [7]:

$$\dot{\lambda}_{x_{ij}} = -\frac{\left(1-\lambda_{x_{ij}}\right)}{J_w.\omega_{ij}^w}\left(\Phi\left(\lambda_{x_{ij}}\right) - Tb_{ij}\right),$$
$$\Phi\left(\lambda_{x_{ij}}\right) = \left(r_{w_{ij}} + \frac{J_w}{r_{w_{ij}}.m_w}\left(1-\lambda_{x_{ij}}\right)\right).fx_{ij}^w \cong r_{w_{ij}}.fx_{ij}^w. \quad (r_{w_{ij}}.m_w \gg J_w) \quad (33)$$

Consequently, the longitudinal slip dynamics for each wheel can be represented by the following dynamical system:

$$\dot{\lambda}_{x_{ij}} = \frac{\left(\lambda_{x_{ij}}-1\right).r_{w_{ij}}.fx_{ij}^w}{J_w.\omega_{ij}^w} + \frac{\left(1-\lambda_{x_{ij}}\right)}{J_w.\omega_{ij}^w}.Tb_{ij} + \Delta_{\lambda,ij}, \left|\Delta_{\lambda,ij}\right| \le l_{\lambda,ij} \quad (34)$$

Within this framework, the upper bound of uncertainties in the aforementioned dynamical system is denoted by $l_{\lambda,ij}$, while the control braking torque for each wheel ($Tb_{ij}$) is designed using the SMC method.

**Theorem 3:** For the nonlinear and uncertain system in (34), selecting a sliding surface $s_{\lambda_{ij}} = \lambda_{x_{ij}} - \lambda_{x_{ij}}^d$ for each wheel and designing the control input (brake torque, $Tb_{ij}^c$) as follows ensures finite-time stability of the lower control layer and, consequently, finite-time tracking of the desired longitudinal slip ($\lambda_{x_{ij}}^d$) determined by the CA layer for each wheel:

$$\dot{\lambda}_{x_{ij}} = \frac{\left(\lambda_{x_{ij}}-1\right).r_{w_{ij}}.fx_{ij}^w}{J_w.\omega_{ij}^w} + \frac{\left(1-\lambda_{x_{ij}}\right)}{J_w.\omega_{ij}^w}.Tb_{ij} + \Delta_{\lambda,ij}, \left|\Delta_{\lambda,ij}\right| \le l_{\lambda,ij} \quad (35)$$

**Proof:** Consider the Lyapunov function denoted by $V_\lambda = \frac{1}{2}\sum_{i=f,r}\sum_{j=r,l} {s_{\lambda_{ij}}}^2$. Taking its derivative and employing (35) along with the substitution of the proposed controller, we obtain:

$$\begin{aligned} \dot{V}_\lambda = \sum_{i=f,r}\sum_{j=r,l} s_{\lambda_{ij}}.\dot{s}_{\lambda_{ij}} \le \\ -\sum_{i=f,r}\sum_{j=r,l}\left(\eta_{\lambda,ij} - l_{\lambda,ij}\right)\left|s_{\lambda_{ij}}\right| \le \\ -\sum_{i=f,r}\sum_{j=r,l}\bar{\eta}_{\lambda,ij}\left|s_{\lambda_{ij}}\right| \le \\ -\sqrt{2}\,\bar{\eta}_\lambda\,V_\lambda^{\frac{1}{2}}, \quad \eta_{\lambda,ij} > l_{\lambda,ij}, \bar{\eta}_{\lambda,ij} = \left(\eta_{\lambda,ij} - l_{\lambda,ij}\right), \bar{\eta}_\lambda = min(\bar{\eta}_{\lambda,ij} - l_{\lambda,ij}) \end{aligned} \quad (36)$$

By implementing the proposed lower-level controller and applying the brake torque $Tb_{ij}^c$ to each wheel, $\dot{V}_\lambda$ becomes negative definite. Consequently, based on its derivative, the considered dynamic system exhibits finite-time stability. Within a finite time $t_r^\lambda \le \frac{\sqrt{2}\,V_\lambda(0)^{\frac{1}{2}}}{\bar{\eta}_\lambda}$, the longitudinal slip of each wheel converges to the desired longitudinal slip $\lambda_{x_{ij}}^d$

## 4. simulation result

To evaluate the designed lateral stability control system, the driver applies the DLC steering scenario (Fig. 6, left) following ESC test reports and ISO-3888 standards. These test conditions are commonly used for assessing lateral stability in production vehicles equipped with ESC. The proposed control algorithm is examined for the desired steering scenarios, assuming a known dry road type and an initial speed of 100 km/h. The control architecture includes the upper layer Smooth- ISMC controller, proposed CA, and lower layer SMC control with the conventional SMC control law. Considering model uncertainties, the control structure accounts for 10% uncertainty in vehicle mass and inertia parameters, approximate lateral tire-road friction forces according to (13), and the term $\Phi\left(\lambda_{x_{ij}}\right)$ in (33) for the lower controller. Additionally, a linear friction model is employed in the CA layer. The proposed control structure, visualized in the legend as "Smooth ISMC", is evaluated through simulation. To benchmark its performance, a three-layer structure with the legend as "SMC", featuring conventional sliding mode control in its upper and lower layers and employing weighted pseudoinverse-based control allocation, is also simulated. The control parameters of each subsystem are presented in Tables I. For linear form (21), the weighted pseudoinverse -based control allocation method proposes the following control signal for each wheel's desired longitudinal slip [17]:

$$u_d = {W_{u_1}}^{-1}B^T(B{W_{u_1}}^{-1}B^T)^{-1}{M_z}^d \quad (37)$$

When the driver applies the sudden steering input to the vehicle, a significant lateral acceleration occurs. However, the ESC system intervenes to prevent the vehicle from deviating from the desired path. Fig. 6 on the right side illustrates the vehicle's trajectory with and without the presence of the ESC system for the two compared control algorithms. While the uncontrolled vehicle exhibits a substantial deviation from the intended trajectory, the proposed control structure outperforms the SMC structure by producing smaller lateral and longitudinal displacements during the specified steering maneuver. The longitudinal and lateral acceleration profiles depicted in Fig. 7 align with the previous observations. The uncontrolled vehicle experiences a dominance of longitudinal acceleration, resulting from lateral force saturation and subsequent instability. The implementation of both the proposed and SMC control systems effectively mitigates this issue by distributing accelerations more evenly. However, the proposed controller demonstrates superior performance in terms of reduced acceleration oscillations.

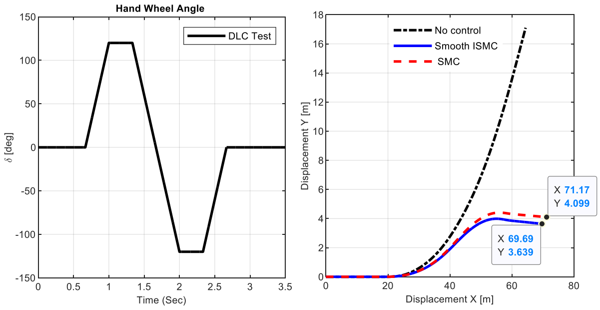


**Fig. 6.** DLC Steering Input Scenario and Vehicle Displacement

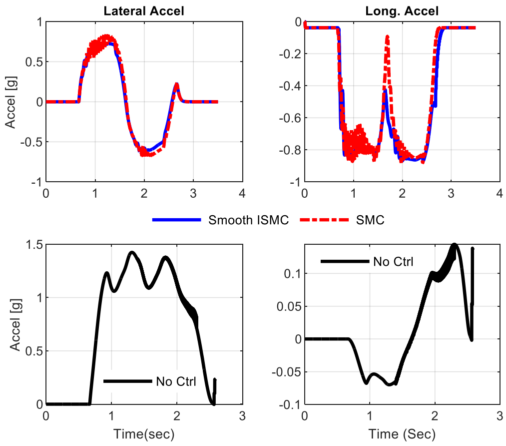


**Fig. 7.** Comparison of vehicle longitudinal and lateral accelerations

Fig. 8 demonstrates that the conventional SMC control algorithm leads to substantial oscillations in wheel angular velocity. In contrast, the proposed control algorithm effectively mitigates these oscillations. Moreover, the classic SMC control can occasionally result in excessive lateral speeds. Conversely, the Smooth SMC control maintains a more stable longitudinal speed profile.

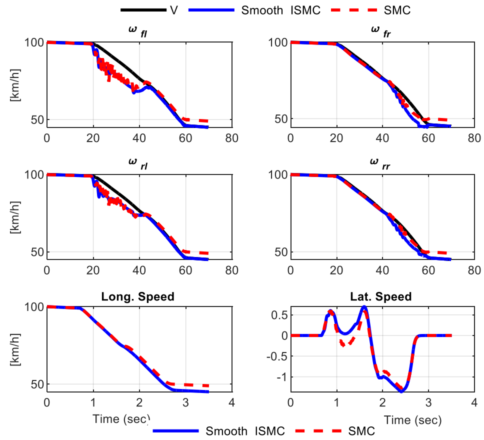


**Fig. 8.** Comparison of Vehicle Speeds (Longitudinal, Lateral) and Wheel Speeds for two Control Strategies

Fig. 9 illustrates desired yaw rate tracking. The conventional SMC algorithm exhibits significant oscillations due to chattering, especially with uncertainties. The proposed control algorithm reduces chattering and improves tracking performance. Notably, after rapid steering inputs, model uncertainties cause significant disturbances, leading to errors in the linear model for lateral forces. As depicted by the $\beta - \dot{\beta}$ trajectories, both control strategies effectively confine the lateral slip angle within the constraints defined by equation (9). Nevertheless, the proposed control algorithm exhibits enhanced stability, as evidenced by the rapid and damped convergence of the $\beta - \dot{\beta}$ trajectory to zero.

The desired longitudinal slip, allocated by the CA layer and tracked by the lower layer, exacerbates chattering in traditional SMC. The proposed Smooth-ISMC effectively mitigates these oscillations, as shown in Fig. 10. Additionally, the inclusion of an integral term in the sliding surface design effectively attenuates the yaw rate error, thereby enhancing the system's steady-state performance. A comparison of the braking torques generated by the two control structures, as shown in Fig. 11, highlights the superior performance of the proposed algorithm in reducing chattering. While both controllers employ SMC at the lower level, the proposed smooth-ISMC-based controller produces smoother brake actuator control signals, indicating a more robust and less oscillatory control action

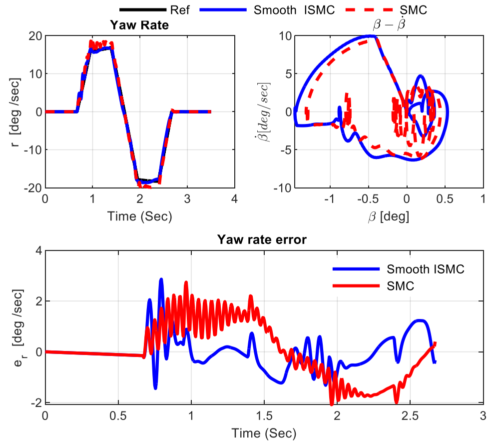


**Fig. 9.** Comparison of Yaw Rate Tracking and Bounedness of Simulated Side Slip Angle for the Smooth-SMC and SMC Algorithms

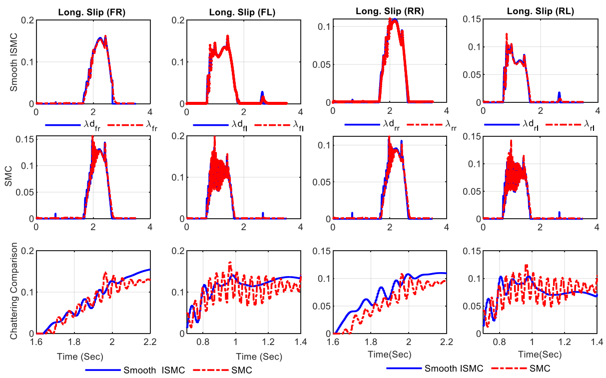


**Fig. 10.** Desired Longitudinal Slip Distribution (Control Allocation) and its tracking by the lower-level controller

The proposed CA successfully fulfills its primary objective of minimizing the discrepancy between the desired vehicle yaw moment and the actual output, as evidenced by the reduced yaw rate error in Fig. 10. Moreover, the secondary objective of minimizing the control signal is also met, as shown by the comparable braking torque profiles in Fig. 11. The convergence of the proposed Lyapunov-based CA to the optimal set $\mathcal{S}_{CA}$, as depicted in Fig. 12, further corroborates its efficacy. The proposed controller's enhanced tracking performance leads to improved vehicle handling and maneuverability, enabling the vehicle to more closely follow the desired trajectory, particularly in challenging driving conditions. By significantly reducing chattering, the controller minimizes wear and tear on the braking system, extending its lifespan and reducing maintenance costs. Additionally, the smoother response of the proposed controller contributes to a more comfortable driving experience for passengers.

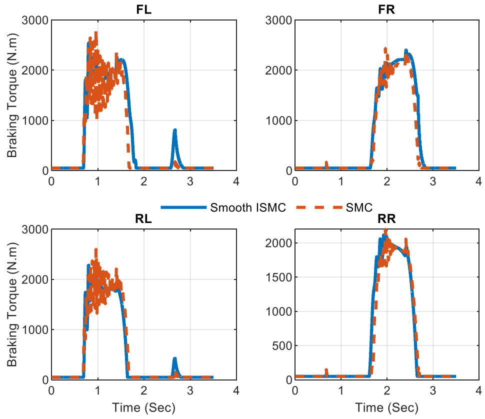


**Fig. 11**. A comparison of the braking torques generated by the lower controller under classical SMC and the novel Smooth SMC algorithms

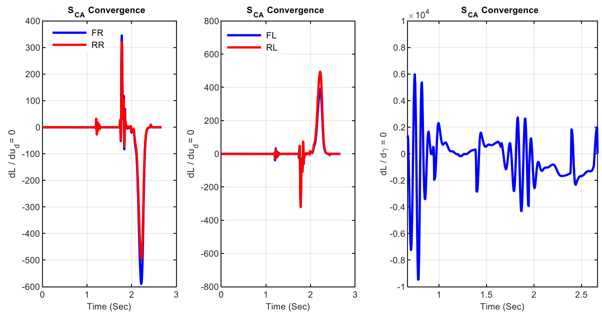


**Fig. 12.** Convergence to the optimal set $\mathcal{S}_{CA}$ in the proposed CA

**Table II: Control algorithms parameters.**

| Control Algorithm | Upper Controller | Control Allocation | Lower Controller |
|---|---|---|---|
| Smooth-ISMC | $\alpha = 1$, $\gamma = 0.75$ $\eta = 15$, $K_I = 245$ | $W_{u_1} = 10\,diag(1,1,3,3)$ $W_{u_2} = 100, k_{CA} = 1$ | $K_{\lambda,ij} = 150$ |
| SMC | $K_r = 55$ | $W_{u_1} = 10\,diag(1,1,1.15,1$ | |

## 5. conclusion

This paper proposes a hierarchical control strategy to enhance vehicle lateral stability. The upper controller employs a smooth integral sliding mode to determine the desired yaw moment A Lyapunov-based analytical solution for dynamic control allocation is presented in the middle layer to distribute the desired longitudinal tire slip. This method guarantees the optimality, convergence, and asymptotic stability of the allocation while offering computational advantages over numerical optimization techniques. The lower controller, utilizing a sliding mode approach, generates braking torque compatible with ABS, akin to traditional ESC systems. Simulation results on a 10-DOF vehicle dynamics model demonstrate improved tracking accuracy, elimination of chattering, and optimal braking torque compared to conventional sliding mode control. Adaptive control algorithms can be explored in future work to further enhance the robustness of the proposed structure and its adaptability to varying road conditions. Furthermore, to enhance the algorithm's performance and accuracy, a disturbance observer can be employed.

## 6. References

[1] M. Asperti, M. Vignati, and E. Sabbioni, "On Torque Vectoring Control: Review and Comparison of State-of-the-Art Approaches", Machines, vol. 12, no. 3, pp. 160, 2024.
[2] A. Lutz, B. Schick, H. Holzmann, et al., "Simulation methods supporting homologation of Electronic Stability Control in vehicle variants", Vehicle System Dynamics, vol. 55, no. 10, pp. 1432-1497, 2017.
[3] V. Mazzilli, De Pinto, et al., "Integrated chassis control: Classification, analysis and future trends," Annual Reviews in Control, vol. 51, pp. 172-205, 2021.
[4] M. Tristano, B. Lenzo, et al., "Hardware-in-the-loop real-time implementation of a vehicle stability control through individual wheel torques", IEEE Transactions on Vehicular Technology, vol. 73, no. 4, pp. 4683-4693, 2024.
[5] J. Hu, Zhang, K. Zhang, P., and F. Yan, "Direct Yaw Moment Control for Distributed Drive Electric Vehicles Based on Hierarchical Optimization Control Framework", Mathematics, vol. 12, no. 11, p. 1715, 2024.
[6] L. Cai, Liao, Z. Wei, S., and J. Li, "Novel direct yaw moment control of multi-wheel hub motor driven vehicles for improving mobility and stability", IEEE Transactions on Industry Applications, vol. 59, no. 1, pp. 591-600, 2022.
[7] E. Muhammad, A. R. Vali, A. Kashaninia, and V. Behnamgol, "Coordination of Active Front Steering and Direct Yaw Control Systems Using MIMO Sliding Mode Control", International Journal of Control, Automation and Systems, vol. 22, no. 1, pp. 1-15, 2024.
[8] I. G. Jang, S. H. You, S. H. Hwang, and W. Cho, "Lateral stability control of a 4-wheel independent drive electric vehicle using the yaw moment contour line concept", IEEE Access, vol. 9, pp. 136892-136904, 2021.
[9] R. Rajamani, Vehicle Dynamics and Control, New York: Springer, 2011, Ch. 8, pp. 201-218.
[10] B. Li, A. Goodarzi, A. Khajepour, S.K. Chen, and B. Litkouhi, "An optimal torque distribution control strategy for four-independent wheel drive electric vehicles", Vehicle System Dynamics, vol. 53, no. 8, pp.1172-1189, 2015.
[11] E. Joa, K. Park, Y. Koh, K. Yi, and K. Kim, "A tyre slip-based integrated chassis control of front/rear traction distribution and four-wheel independent brake from moderate driving to limit handling", Vehicle System Dynamics, vol. 56, no. 4, pp. 579-603, 2018.
[12] Y. Zhang, J. Ma, and Y. Zhou, "Adaptive Nonsingular Fast Terminal Sliding Mode-Based Direct Yaw Moment Control for DDEV under Emergency Conditions", Actuators, vol. 13, no. 5, pp. 170, 2024.
[13] N. Guo, Z. Xudong, Z.Yuan, L. Basilio, Tao Zhang, and G. Dietmarm, "A fast model predictive control allocation of distributed drive electric vehicles for tire slip energy saving with stability constraints", Control Engineering Practice, vol. 102, pp. 104554, 2020.
[14] L. Chen, L. Zhiqiang, Y. Juanjuan, and S. Yu, "Lateral stability control of four-wheel-drive electric vehicle based on coordinated control of torque distribution and ESP differential braking", Actuators, vol. 10, no. 6, p. 135. MDPI, 2021.
[15] J. Tjønnås, Tor A. Johansen, "Adaptive control allocation", Automatica, vol. 44, no. 11, pp. 2754-2765, 2008.
[16] Y. Chen and J. Wan, "Adaptive Energy-Efficient Control Allocation for Planar Motion Control of Over-Actuated Electric Ground Vehicles", IEEE Transactions on Control Systems Technology, vol. 22, no. 4, pp. 1362-1373, 2014.
[17] M. Mirzaei, A.R. Vali, F. Allahverdizadeh, V. Behnamgol, "Fixed-time dynamic control allocation for the distribution of braking forces in a vehicle ESC system", Nonlinear Dynamics, 2024. https://doi.org/10.1007/s11071-024-10168-y.Z.
[18] Z. Kang, Q. Shen, S. Wu, and C.J. Damaren, "Prescribed Performance-Based Fixed-Time Adaptive Control Allocation for Overactuated Spacecraft, " Journal of Guidance, Control, and Dynamics, vol. 46, no. 2, pp. 390-400, 2023.
[19] R. de Castro, and B. Jonathan, "Lyapunov-based fault tolerant control allocation, " Vehicle System Dynamics, vol. 60, no. 10, pp. 3605-3630, 2022.
[20] Z. R. M. Júnior, A. Murilo, and R. V. Lopes, "Vehicle stability upper-level-controller based on parameterized model predictive control", IEEE Access, vol. 10, pp. 21048-21065, 2022.
[21] E. Muhammad, A. R. Vali, A. Kashaninia, and V. Bahnamgol, "Stability enhancement of hybrid electric vehicles using optimal fuzzy logic", International Journal of Dynamics and Control, vol. 12, no. 4, pp. 1130-1145, 2024.
[22] X. Sun, Y. Wang, Y. Cai, P. K. Wong, and L. Chen, "NFTSM control of direct yaw moment for autonomous electric vehicles with consideration", Math. Biosci. Eng., vol. 20, no. 7, pp. 13334-13355, 2023.
[23] Z. Wang, J. Zhu, L. Zhang, and Y. Wang, "Automotive ABS/DYC coordinated control under complex driving conditions", IEEE Access, vol. 6, pp. 32769-32779, 2018.
[24] M. Ehsani, A. Oraee, B. Abdi, V. Behnamgol, and M. Hakimi, "Adaptive dynamic sliding mode controller based on extended state observer for brushless doubly fed induction generator", International Journal of Dynamics and Control, pp.1-14, 2024.
[25] J. Liu, L. Gao, J. Zhang, and F. Yan, "Super-twisting algorithm second-order sliding mode control for collision avoidance system based on active front steering and direct yaw moment control", Proceedings of the Institution of Mechanical Engineers, Part D: Journal of Automobile Engineering, vol. 235, no. 1, pp. 43-54, 2021.
[26] L. Ma, C. Cheng, et al., "Direct yaw-moment control of electric vehicles based on adaptive sliding mode", Math. Biosci. Eng., vol. 20, no. 7, pp. 13334-13355, 2023.
[27] U. Kiencke and L. Nielsen, Automotive Control Systems: For Engine, Driveline, and Vehicle, Berlin: Springer, 2000, Ch. 8, pp. 301-350.
[28] M. Ehsani, A. Oraee, B. Abdi, V. Behnamgol, and M. Hakimi, "Adaptive Dynamic Sliding Mode Algorithm for BDFIG Control", Iranian Journal of Electrical & Electronic Engineering, 19(1), 2023.
[29] M. Ali Akbar Semnani, A. R. Vali, S. M. Hakimi, and V. Behnamgol, "Modelling and design of observer-based smooth sliding mode controller for heart rhythm regulation", International Journal of Dynamics and Control, pp. 1-5, 2021.
[30] J. Nocedal and S. Wright, "Numerical Optimization, New York, Springer, " Ch. 16, pp. 451-453, 2006.